

Modelling Prostate Gland Motion for Image-Guided Interventions

Yipeng Hu¹, Dominic Morgan¹, Hashim Uddin Ahmed², Doug Pendsé^{3,4}, Mahua Sahu³, Clare Allen⁴, Mark Emberton², David Hawkes¹, and Dean Barratt¹

¹ Centre for Medical Image Computing, Department of Medical Physics & Bioengineering;

² Department of Urology, Division of Surgery & Interventional Science; and

³ National Medical Laser Centre, University College London, London, UK

⁴ Department of Radiology, University College Hospital, London, UK

Abstract. A direct approach to using finite element analysis (FEA) to predict organ motion typically requires accurate boundary conditions, which can be difficult to measure during surgical interventions, and accurate estimates of soft-tissue properties, which vary significantly between patients. In this paper, we describe a method that combines FEA with a statistical approach to overcome these problems. We show how a patient-specific, statistical motion model (SMM) of the prostate gland, generated from FE simulations, can be used to predict the displacement field over the whole gland given sparse surface displacements. The method was validated using 3D transrectal ultrasound images of the prostates of five patients, acquired before and after expanding the balloon covering the ultrasound probe. The mean target registration error, calculated for anatomical landmarks within the gland, was 1.9mm.

Keywords: Biomechanical modelling, finite element analysis, image-guided interventions, prostate cancer, ultrasound, statistical shape modelling.

1 Introduction

Transrectal ultrasound (TRUS) imaging is used routinely to guide needle biopsy of the prostate gland as well as therapeutic interventions for prostate cancer. However, conventional (B-mode) TRUS is two-dimensional and provides very limited information on the spatial location of tumours. Consequently, performing accurate, targeted biopsy and therapy using TRUS guidance alone is practically difficult, especially for the inexperienced practitioner. The ability to fuse additional information on tumour location, derived from magnetic resonance (MR) imaging or a previous biopsy, with TRUS images during a procedure therefore represents a major step towards improving the accuracy of image-guided interventions for prostate cancer, particularly as the sensitivity and specificity of functional and structural MR imaging techniques for detecting and localising prostate cancer continue to improve [1]. The fusion of detailed 3D information on the spatial location of tumours and realtime TRUS images acquired during a procedure potentially enables targeted biopsy sampling and therapies, such as radio-, brachy- and cryotherapy and, high-intensity focused US (HIFU), to be delivered at a precise location, thus avoiding important structures and minimising the risk of side effects.

Largely due to the very different intensity characteristics between MR and US images of the prostate (especially those arising from US-specific artefacts), automatic, intensity-based image registration techniques perform poorly in general. Feature-based methods are also of limited value because of the difficulty associated with extracting anatomical features from TRUS images without significant user interaction, which renders such techniques impractical in the clinical situation due to time constraints. The fact that the prostate is a deformable organ is also problematic as this means that the assumption of a rigid-body motion does not hold. Significant gland motion (including deformation) commonly takes place due to forces exerted by the bladder and rectum, patient position (e.g. supine versus lithotomy), and the placement of an US probe or MR coil into the rectum [2]. Potentially large changes in gland volume can also occur during and following interventions as a physiological response to needle insertion, ablative therapy, or both (but these sources of motion are not considered in this paper).

We have recently reported on a hybrid approach in which a patient-specific 3D model of the prostate surface (capsule), derived from an MR image, is registered automatically to 3D TRUS images [3], but the accuracy and robustness of this technique is limited by the assumption that the gland remains rigid between MR and TRUS image acquisitions. Moreover, there remains the problem of how best to estimate tissue motion within the gland given information on the motion of the gland surface. Biomechanical modelling, based on finite element analysis (FEA), has been proposed as a potential method for predicting deformation within the prostate gland [4]–[8], but, when applied directly, this method requires accurate boundary conditions, such as the displacement of the gland surface and the TRUS probe/balloon, and accurate estimates of the elastic properties of the soft tissue within the anatomical region of interest. In practice, however, considerable uncertainty exists in these parameters since typically only limited boundary condition data are available from TRUS imaging during an intervention, and the material properties are known to vary considerably between different tissue types and between patients. Chi et al., for example, report a registration error of up to 4.5mm due solely to a 30% uncertainty in material properties for a linear FE model of the prostate [4]. A patient-specific dependency on material properties is also reported for both linear and non-linear biomechanical breast tissue models [9]. Furthermore, the computation time increases rapidly with the complexity of the FE model, which can make FEA methods impractical in the surgical situation and inevitably leads to a trade-off between model accuracy and efficiency. Although dramatic reductions in computation time can be achieved using, for example, graphical processor units [10], standard FEA methods for computing deformations in heterogeneous soft-tissue are still too slow to be usefully implemented within an iterative optimisation scheme, such as the one described in this paper, which addresses the uncertainties in boundary conditions and material properties.

Here, we adopt an approach originally proposed by Davatzikos et al. [11] in which biomechanical modelling is used to simulate physically plausible gland deformations under different boundary conditions and with variable material properties. The resulting deformed prostate models are then used to train a statistical model in order to generate a compact and computationally efficient model of prostate motion that is sufficiently fast to predict an intra-gland deformation field during a surgical procedure. An important advantage of this approach is that the allowed deformation of the

resulting motion model is sufficiently constrained to enable the model to be fitted to sparse measurements of the displaced gland surface, which can be practically obtained from a small number of TRUS images, acquired during an intervention.

Mohamed et al. [5] previously applied this approach to construct a statistical deformation model of a phantom prostate gland using FE simulations with variable position and orientation of the (virtual) TRUS probe as training examples. In our work, the material properties assigned to different tissue regions are also varied in the bio-mechanical simulations, thus relaxing the requirement for accurate knowledge of these properties and enabling a much greater range of physically plausible deformations to be captured. In the work of Alterovitz et al. [6], the intra-gland deformation field, material properties and external forces are all estimated using FEA and a geometric model based on 2D MR images. However, to the best of our knowledge, the present study is the first to report on the validation of a fully 3D model of prostate motion based on FEA and *in vivo* image data, which takes into account uncertainties in material properties and the sparseness of boundary condition data that are typically available during TRUS-guided interventions.

2 Methods

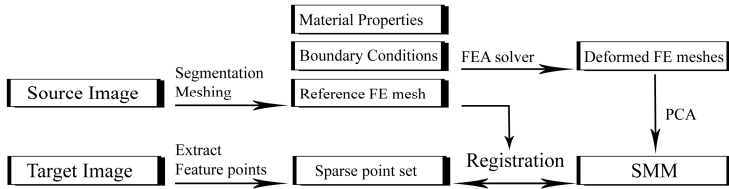


Fig. 1. Overview of the method described in this paper (see text for details). In this study, the source and target images were 3D TRUS images acquired before and after expanding the saline-filled balloon covering the TRUS probe, respectively.

2.1 Overview

A schematic overview of the method developed in this work is shown in Fig. 1. The steps involved are summarised as follows:

- Segment the prostate gland, rectal wall, and (if visible) the pelvic bone, from the source image. (For the purposes of this study, manual segmentation was used, although, in principle, any segmentation method could be applied.)
- From the segmented source image, build a patient-specific, 3D, reference FE mesh of the prostate gland, the rectal wall, the TRUS balloon (which ordinarily ensures acoustic coupling between the rectal wall and US transducer), and the pelvic bone.
- Perform a large number of FEA simulations using randomly assigned material properties and boundary conditions, which correspond to different positions, orientations, and diameters of the balloon within the rectum that might be encountered during a TRUS-guided procedure.

- d) Apply principal component analysis (PCA) to a set of vectors containing the simulated displacements of the node points of the gland in the FE mesh and the boundary condition parameters (which in this case define the pose and diameter of the balloon). A statistical motion model (SMM) is then formed from the principal modes of variation and constrains the deformation of the gland surface model.
- e) Identify points on the surface of the gland and TRUS balloon in the target image.
- f) Register the deformable gland model to the target surface points by optimising the weights of the principal modes of variation of the SMM such that the distance between the target point set and the deformed model surface is minimised. The measured diameter of the balloon in the target image is used as a further numerical constraint in this optimisation.

In order to provide an accurate gold standard for validation without implanted fiducial markers, in this study both the source and target images were 3D TRUS images. However, it is intended that in clinical practice the source image would most likely be a MR image, acquired prior to an intervention, although a CT image might also be used for radio- or brachytherapy applications. Step (a) may require significant user interaction to accurately segment the source image, whilst steps (b) and (c) are computationally intensive. Therefore, in practice, steps (a)-(d) would be performed before a procedure, whereas steps (e) and (f) would take place during the procedure (in realtime). Details of the experimental methods used to implement and validate the method outlined above are provided in the following sections.

2.2 3D TRUS Volume Acquisition

Three-dimensional TRUS images of the prostate were acquired for 5 patients undergoing a template-guided biopsy, HIFU therapy, or photodynamic therapy (PDT) for treatment of prostate cancer. All patients were recruited to clinical research studies at University College Hospital, and gave written, informed consent to participate in studies approved by the local research ethics committee. In the case of biopsy and PDT, a set of parallel transverse B-mode US images was obtained using a B-K Pro-Focus scanner (B-K Medical, Berkshire, UK) and a mechanical stepper mechanism (Tayman Medical Inc., MO, USA) to translate the probe (B-K 8658T, 5-7.5MHz transducer) axially along the rectum. Images were captured at 2mm intervals and stored on the US scanner. In the case of HIFU therapy, 3D volumes were acquired automatically using a Sonablate® 500 system (Focus Surgery, Inc., Indiana, USA). Two volumes were acquired for each patient at the start of the procedure: one with the balloon at minimal expansion, and the other after expanding the balloon by injecting saline with a syringe in order to deform the prostate gland. Expanding the balloon in this way simulates the motion of the prostate gland that might typically occur due to the presence of a TRUS probe or an endorectal MR imaging coil. The first volume was chosen as the source image for building the SMM, whilst the second (target image) was used for accuracy evaluation.

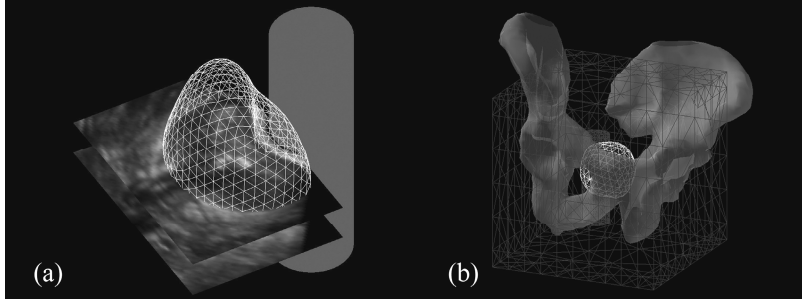


Fig. 2. (a) A triangulated surface mesh and cylinder, representing the prostate gland surface and TRUS balloon surfaces, respectively. (b) A generic model of the pelvic bone surface shown relative to the prostate gland in the FE mesh.

2.3 Finite Element Model Construction

The prostate gland was segmented in both the source and target 3D TRUS volumes by manually contouring the capsule on the acquired transverse slices. Because of known differences in compressibility between anatomical zones in the prostate, the gland was further segmented into an inner and outer gland, based on differences in echotexture on the US images [7]. A smooth surface was fitted to the surface contour points using a spherical harmonic representation from which a triangulated mesh was generated as shown in Fig. 2a. The surface of the balloon was modelled as a cylinder. The reference diameter and position of the cylinder was determined automatically by performing a least squares fit to points on the balloon surface, extracted from the original 2D TRUS images using a Canny edge detection filter. The tissue surrounding the prostate was modelled as a homogeneous block with dimensions $20 \times 20 \times 20 \text{ cm}^3$.

The surface meshes and the block structure were imported into the commercial FEA software ANSYS (ANSYS Europe Ltd., Oxfordshire, UK). A FE mesh was then constructed and automatically meshed into ten-noded tetrahedral elements using trimmed parametric surfaces and Delaunay tessellation techniques provided by the software. Ten-noded tetrahedral elements were chosen because of their flexibility to generate unstructured meshes, which enables non-linear geometries to be simulated and a quadratic shape function to be employed to improve accuracy. Models for each patient consisted of between 30,000 to 40,000 elements. No badly shaped elements were generated during the model construction process. Regions corresponding to each part of the prostate gland, the rectal wall, and surrounding tissue were labelled separately and assigned different material properties (see below). All tissues were assumed to behave as isotropic, linear elastic materials. Deformations were computed using the ANSYS implementation of a pre-conditioned conjugate gradient (PCG) iterative equation solver with automatic time stepping turned on.

2.4 Boundary Conditions and Material Properties

For each case, 500 FEA simulations of prostate motion were performed using ANSYS with randomly assigned material properties and boundary conditions corresponding to different balloon (cylinder) diameters and poses. The ranges of the material properties

Table 1. Summary of the boundary conditions and material properties used for the FEA simulations. $*R_0$ denotes the radius of the balloon measured from the source image. **The subscripts 1-4 correspond to the inner prostate gland (1), the outer prostate gland (2), the rectal wall (3), and the surrounding tissue (4), respectively. ***The rectal wall in contact with the balloon is assumed to be nearly incompressible – i.e., $\nu_3 = 0.49$.

Description	Parameter(s)	Range	Reference Value(s)	DOF
Balloon radius	R	$[0.9R_0, 1.5R_0]^*$	R_0	1
Balloon translation	T_x, T_y, T_z	$[-5, 5]$ mm	$T_x = T_y = T_z = 0$ mm	3
Balloon rotation	$\theta_x, \theta_y, \theta_z$	$[-10, 10]$ °	$\theta_x = \theta_y = \theta_z = 0^\circ$	3
Young's modulus	E_1, E_2, E_3, E_4^{**}	$[10, 200]$ kPa	–	4
Poisson's ratio	$\nu_1, \nu_2, \nu_4^{***}$	$[0.30, 0.49]$	–	3***

used, given in Table 1, correspond to ranges of values reported in literature (e.g. [4]). Since the assumption of incompressibility (Poisson's ratio, $\nu = 0.5$) is arguably not appropriate for the prostate gland because of the likelihood of fluid loss and collapse of the urethra under compression (which explain observed changes in volume) values for both the Young's modulus and the Poisson's ratio were assigned randomly for each simulation. The expansion of the balloon was modelled by applying a radial displacement to the cylinder surface nodes. The precise position and orientation of the TRUS probe in the rectum is unknown prior to a procedure and therefore the cylinder representing the balloon surface was repositioned in each simulation by applying a random rigid-body transformation. The values of all random variables were drawn from a uniform probability distribution with upper and lower limits set by the ranges given in Table 1. In the case of the Young's modulus, only the relative values of this property are relevant.

Because only a very small part of the pelvic bone is visualised in TRUS images, it was not possible to accurately estimate its shape or location relative to the prostate (although this would be possible if MR or CT was used as the source image). For this reason, a surface model of an average male pelvis, derived from CT images [12], was used to fix the FE mesh node positions at the bone surface. The position and orientation of the bone relative to the prostate was determined using the method described in [13] (see Fig. 2b).

2.5 Statistical Motion Model

For each of M ($=500$) simulated gland deformations, the 3D displacement of every node in the prostate gland mesh was calculated. The components of these displacements were combined with the balloon radius and rigid-body parameters to form a vector, \mathbf{x} , defined (for the i^{th} simulation) as:

$$\mathbf{x}_i = [\delta_1^T, \delta_2^T, \dots, \delta_N^T, R, T_x, T_y, T_z, \theta_x, \theta_y, \theta_z]_i^T, \quad 1 \leq i \leq M \quad (1)$$

where N is the number of gland mesh nodes, $\delta_j^T = [\delta_x, \delta_y, \delta_z]_j$ is the 3D displacement vector for node j ($1 \leq j \leq N$), and the remaining parameters define the radius, position and orientation of the balloon, respectively (see Table 1). The principal modes of variation in \mathbf{x} were then calculated by finding the principal eigenvectors of the covariance matrix, \mathbf{C} , given by:

$$\mathbf{C} = \frac{1}{M-1} \sum_{i=1}^M (\mathbf{S}\mathbf{x}_i - \bar{\mathbf{x}})(\mathbf{S}\mathbf{x}_i - \bar{\mathbf{x}})^T, \quad \bar{\mathbf{x}} = \frac{1}{M} \sum_{i=1}^M \mathbf{S}\mathbf{x}_i \quad (2)$$

In (2), \mathbf{S} is a diagonal scaling matrix in which the diagonal element $\mathbf{S}_{kk} = 1/\sigma_k$, where σ_k is the standard deviation of the M values for the k^{th} element of \mathbf{x} ($1 \leq k \leq 3N+7$). Now, if \mathbf{e}_i is the eigenvector corresponding to the i^{th} largest eigenvalue of \mathbf{C} , and c_i is a scalar weight, the new mesh node co-ordinates of a deformed prostate model, contained in vector \mathbf{p} , can be reconstructed using:

$$\mathbf{p} = \mathbf{p}_0 + \mathbf{S}^{-1} \left(\bar{\mathbf{x}} + \sum_{i=1}^L c_i \mathbf{e}_i \right), \quad 1 \leq L \leq M \quad (3)$$

where \mathbf{p}_0 contains the gland node co-ordinates in the reference mesh (derived from the source image) and the reference balloon parameters. For any $L < M$, the RMS model reconstruction error for one training simulation can be defined as:

$$\varepsilon = \sqrt{\frac{1}{n} \left(\sum_{i=L+1}^M c_i \mathbf{S}^{-1} [\mathbf{e}_i]_{(a,b)} \right)^T \left(\sum_{i=L+1}^M c_i \mathbf{S}^{-1} [\mathbf{e}_i]_{(a,b)} \right)} \quad (4)$$

where $[\mathbf{e}_i]_{(a,b)}$ denotes the vector formed from the elements a through to b of eigenvector \mathbf{e}_i . If $a = 1$ and $b = n = 3N$, evaluating (4) gives the RMS error in the gland node displacements, denoted here by $\varepsilon_{\text{gland}}$. Similarly, we can define a reconstruction error, ε_R , for the balloon radius, R , by setting $a = b = 3N+1$ and $n = 1$. In this study, L was chosen so that the SMM covered $> 99\%$ of variance in the training data and that $\varepsilon_{\text{gland}} < 0.5\text{mm}$ and $\varepsilon_R < 0.5\text{mm}$, computed over all training examples.

2.6 Model Registration

Since an accurate manual 3D segmentation of the prostate surface in the target TRUS image is impractical during a procedure, a simple, clinically feasible protocol for defining a sparse set of target points was simulated in which the segmented target gland surface was resliced in 3 sagittal and 3 transverse planes, corresponding to 6 different TRUS views. Then, 6 evenly spaced points were computed on the surface contours in each slice, yielding 36 target points in total. Initial estimates for the weights, $[c_1, c_2, \dots, c_L]$, were computed by solving Eq. (3) with $\mathbf{p} = [[\mathbf{p}_0]_{(1,3N)}, R_{\text{target}}, [\mathbf{p}_0]_{(3N+2,3N+7)}]^T$, where R_{target} is the balloon radius measured automatically in the target TRUS image. The optimal weights were then estimated using a quasi-Newton, nonlinear least-squares algorithm provided in the MATLAB Optimization Toolbox (The Mathworks Inc., MA, USA), which minimises the distance between the target points and the deformed model gland surface with the constraint $\|[\mathbf{p}]_{(3N+1)} - R_{\text{target}}\| < 0.5\text{mm}$. Once registered, the positions of any point inside the deformed gland can be calculated by interpolating the displaced node point positions. For the purposes of comparison with a rigid registration algorithm, the source (i.e., undeformed) surface was registered to the target points using the well-known iterative closest point (ICP) algorithm.

2.7 Accuracy Validation

A number of corresponding landmarks, including cysts, calcifications and the urethra, were identified manually in the source and target TRUS volumes. The landmarks in the source image were then propagated into the target image space using the displacement field produced by the SMM following registration. For each pair of landmarks, a target registration error (TRE) was calculated, defined as the distance between manually defined and propagated landmark in the target image space.

Table 2. Target registration errors calculated for anatomical landmarks. L is the number of principal eigenmodes used in the SMM (see Equation (3)).

Case No.	Number of Landmarks	L (Variance (%))	Mean±SD TRE (mm)		
			Start	Rigid	SMM
1 (Biopsy)	12	26 (99.89 %)	5.45 ± 1.16	3.32 ± 0.98	1.86±0.76
2 (PDT)	7	28 (99.95 %)	4.32 ± 1.39	2.59 ± 0.50	1.43±0.41
3 (HIFU)	8	23 (99.92 %)	5.03 ± 0.78	2.23 ± 1.28	2.15±1.33
4 (Biopsy)	15	24 (99.92 %)	4.47 ± 1.02	2.63 ± 0.77	1.84±1.19
5 (HIFU)	6	24 (99.92 %)	6.42 ± 1.48	3.73 ± 0.98	2.27±2.22
All	48		5.03 ± 1.29	2.87 ± 1.01	1.89±1.19

3 Results

The landmark-based TREs are given in Table 2. All registrations were completed within 10s on a PC with a 2.33GHz Intel® Core™ dual CPU processor and 3GB of RAM. The time taken to compute each SMM was between 30 and 50 hours using the same computer. Inspection of the results in Table 2 reveals that in all cases the lowest TREs were achieved by using the SMM to constrain the deformable surface registration. Although a significant proportion of gland motion (~40%) was recovered using a rigid registration scheme, the SMM-constrained deformable registration recovered over 60% of the motion on average, depending on the proportion of gland deformation.

4 Discussion

The approach described in this study combines statistical motion modelling techniques with FEA to generate patient-specific, 3D deformable models of the prostate gland that deform in a manner that is physically plausible, but sufficiently well constrained that only a small number of surface points, derived from standard TRUS views, are required for registration. Since such a model can be generated before an intervention, does not require accurate estimates of material properties or intraoperative boundary conditions, such as the exact pose of the TRUS probe, and can be rapidly registered to target surface points, this method is clinically feasible.

For this study we used a commercial FEA package (ANSYS), which supports non-linear geometry, and a linear elastic constitutive model to calculate gland deformations. Although such a model involves simplifying assumptions on the biomechanical

behaviour of soft-tissue, an SMM based on a linear elastic biomechanical model (but non-linear geometry), resulted in a reduction in TRE in all of the cases in this study compared with a simple rigid registration scheme (see Table 2). To investigate the effect of varying material properties on the predicted gland displacements, we computed, for each node in each patient model, the Euclidean distance between each displaced node position, calculated using 10 different sets of randomly assigned Young's modulus and Poisson's ratio and fixed boundary conditions ($R=1.5R_0$; $T_x=T_y=T_z=0\text{mm}$; $\theta_x=\theta_y=\theta_z=0^\circ$), and the mean of these 10 displaced node positions. The mean value of the maximum distance (from the 10 displacements computed for each node) was 1.82mm, whilst the maximum distance was 3.85mm. These results indicate that varying the material properties has a significant effect on the displacements predicted using the biomechanical model used in this study, given that the average magnitude of the tissue displacement due to expanding the balloon was approximately 5mm (see Table 2).

Further work is required to investigate the accuracy of generating an SMM from another imaging modality, such as MR. In this case, the diameter, position and orientation of the TRUS balloon are unknown before a procedure, but we have shown how such parameters can be estimated during the registration, given an automatically measured estimate of balloon diameter. It may also be possible to obtain estimates of the other parameters during a procedure, for example, by measuring the position and orientation of the TRUS probe using a 3D tracking device, and use these measurements to further constrain the registration optimisation. The use of 3D TRUS images to build a "preoperative" SMM provided a convenient framework for the purposes of validation, since anatomical landmarks visible in the TRUS images could be accurately tracked as the balloon was expanded. In future work, we intend to use MR images to build SMMs, which raises the problem of accurately establishing corresponding landmarks within the prostate gland. This problem could be overcome by using implanted fiducial markers as targets for evaluating the registration accuracy.

Acknowledgments. The Authors would like to thank Zeike Taylor, Christine Tanner and Tim Carter for their advice on aspects of biomechanical modelling. Dean Barratt is funded as a Royal Academy of Engineering /EPSRC Research Fellow.

References

1. Kirkham, A.P., et al.: How good is MRI at detecting and characterising cancer within the prostate? *Eur. Urol.* 50, 1163–1174 (2006)
2. Byrne, T.E.: A review of prostate motion with considerations for the treatment of prostate cancer. *Medical Dosimetry* 30, 155–161 (2005)
3. Morgan, D., et al.: Registration of preoperative MR to intraoperative ultrasound images for guiding minimally-invasive prostate interventions. In: *Proc. MIUA*, pp. 181–185 (2007)
4. Chi, Y., et al.: A material sensitivity study on the accuracy of deformable organ registration using linear biomechanical models. *Med. Phys.* 33, 421–433 (2006)
5. Mohamed, A., et al.: A combined statistical and biomechanical model for estimation of intra-operative prostate deformation. In: Dohi, T., Kikinis, R. (eds.) *MICCAI 2002. LNCS*, vol. 2489, pp. 452–460. Springer, Heidelberg (2002)

6. Alterovitz, R., et al.: Registration of MR prostate images with biomechanical modeling and nonlinear parameter estimation. *Med. Phys.* 33, 446–454 (2006)
7. Bharatha, A., et al.: Evaluation of three-dimensional finite element-based deformable registration of pre-and intraoperative prostate imaging. *Med. Phys.* 28, 2551–2560 (2001)
8. Crouch, J.R., et al.: Automated finite element analysis for deformable registration of prostate images. *IEEE Trans. on Med. Imag.* 26, 1379–1390 (2007)
9. Tanner, C., et al.: Factors influencing the accuracy of biomechanical breast models. *Med. Phys.* 33, 1758–1769 (2006)
10. Taylor, Z.A., et al.: Real-time nonlinear finite element analysis for surgical simulation using graphics processing units. In: Ayache, N., Ourselin, S., Maeder, A. (eds.) *MICCAI 2007, Part I. LNCS*, vol. 4791, pp. 701–708. Springer, Heidelberg (2007)
11. Davatzikos, C., et al.: A framework for predictive modelling of anatomical deformations. *IEEE Trans. Med. Image* 20, 836–843 (2001)
12. Thompson, S., et al.: Use of a CT statistical deformation model for multi-modal pelvic bone segmentation. In: *Proc. SPIE Medical Imaging* (2008)
13. Schallenkamp, J., et al.: Prostate position relative to pelvic bony anatomy based on intra-prostatic gold markers and electronic portal imaging. *Int. J. Radiation Oncology Biol. Phys.* 63, 800–811 (2005)